Steel and Composite Structures, *Vol. 30, No. 4 (2019) 337-350*
DOI: https://doi.org/10.12989/scs.2019.30.4.337

Confinement coefficient of concrete-filled square stainless steel tubular stub columns

Fa-xing Ding [1,2], Yi-xiang Yin [1], Liping Wang [*1,2], Yujie Yu [1], Liang Luo [1] and Zhi-wu Yu [1,2]

[1] *School of Civil Engineering, Central South University, Changsha, Hunan Province, 410075, PR China*
[2] *Engineering Technology Research Center for Prefabricated Construction Industrialization of Hunan Province, 410075, PR China*

(*Received July 13, 2018, Revised November 4, 2018, Accepted February 18, 2019*)

Abstract. The objective of this paper is to investigate the confinement coefficient of concrete-filled square stainless steel tubular (CFSSST) stub columns under axial loading. A fine finite 3D solid element model was established, which utilized a constitutive model of stainless steel considering the strain-hardening characteristics and a triaxial plastic-damage constitutive model of concrete with features of the parameter certainty under axial compression. The finite element analysis results revealed that the increased ultimate bearing capacity of CFSSST stub columns compared with their carbon steel counterparts was mainly due to that the composite action of CFSSST stub columns is stronger than that of carbon steel counterparts. A further parametric study was carried out based on the verified model, and it was found that the stress contribution of the stainless steel tube is higher than the carbon steel tube. The stress nephogram was simplified reasonably in accordance with the limit state of core concrete and a theoretical formula was proposed to estimate the ultimate bearing capacity of square CFSSST stub columns using superposition method. The predicted results showed satisfactory agreement with both the experimental and FE results. Finally, the comparisons of the experimental and predicted results using the proposed formula and the existing codes were illustrated.

Keywords: square stainless steel tube; finite element analysis; composite action; ultimate bearing capacity; confinement coefficient

1. Introduction

Over the past several decades, stainless steel has been increasingly used in building constructions and city bridges around the world. Due to its superior corrosion resistance, good ductility, aesthetics appearance, easy maintenance and low cost in the whole life cycle, stainless steel has been applied to quite a few famous projects, such as the Siena Bridge in Italy, the Stonecutters Bridge Towers in Hong Kong, the Marina Bay in Singapore, US Air Force Memorial in Washington DC, USA, and the Likholefossen Bridge in Norway etc. (Gedge 2008). Attributing to the virtues of stainless steel, it is foreseeable that stainless steel will be increasingly employed in architectural engineering, bridge engineering and offshore structures.

Up to now, a number of experimental and numerical studies have been conducted on the concrete-filled steel tubular (CFT) columns (Evirgen *et al*. 2014, Yang *et al*. 2016, Lume *et al*. 2017, Li *et al*. 2015, Wan and Zha 2016, Pons *et al*. 2018). However, the investigation for concrete-filled stainless steel tubular (CFSST) stub columns is still limited. A series of test studies have been accomplished and the mechanical performance of CFSST stub columns with square and circular cross-sections were investigated (Uy *et al*. 2011, Lam and Gardner 2008). The different types of concrete filled stainless steel tube were also studied, such as polypropylene fibre reinforced concrete (Ellobody and Ghazy 2013) and recycled aggregate concrete (Tam *et al*. 2014). Liao *et al*. (2016) reported the hysteretic behaviour of CFSST columns based on the experimental study results and the fire performance of concrete-filled stainless steel tubular columns were also discussed (Han *et al*. 2013). The numerical investigations were presented on square CFSST stub columns (Tao *et al*. 2011) and circular CFSST stub columns (Patel *et al*. 2014).

To sum up, the tests and numerical investigations on mechanical behavior of CFSST columns have been investigated in the existing research. However, the previous numerical simulation mainly discussed the factors having influence on the mechanical behavior of CFSST columns under axial load. The confinement coefficient of the square CFSST stub columns were rarely investigated and the different composite action between CFSST stub columns and low carbon steel CFT stub columns were never discussed before.

Therefore, this study focused on the confinement coefficient of square CFSST stub columns and difference in the composite action between square CFSST stub columns and low carbon steel CFT stub columns. The main contents of this paper include: (1) A fine finite 3D solid element model of square CFSSST stub columns was established by adopting a constitutive model of stainless steel considering the strain-hardening characteristics and a triaxial plastic-damage constitutive model of concrete under axial compression proposed by the research group, and non-linear finite element analysis was carried out to simulate the

∗Corresponding author, Ph.D.,
E-mail: wlp2016@csu.edu.cn

ISSN: 1229-9367 (Print), 1598-6233 (Online)

whole loading process of CFSSST stub columns. (2) Based on the verified model, a parametric study was performed and the composite action difference between the CFSSST stub columns and the square low carbon steel CFT stub columns was discussed. Finally, based on the superposition method, a practical design formula considering the confinement coefficient was proposed to predict the ultimate bearing capacity of the CFSSST stub columns and the proposed design model has higher accuracy through comparing with the existing formulas in current design codes.

2. Finite element modeling

2.1 Finite element models

Non-linear finite element models for CFSSST columns under axial compression were established using ABAQUS version 6.14 (2014). In the numerical models, the 8-node reduced integral format 3D solid element (C3D8R) was applied to model the stainless steel tube, core concrete and loading plates for all specimens. The structured meshing technique was adopted as shown in Fig. 1.

The surface-to-surface contact was adopted for the interaction between stainless steel tube and core concrete, in which the inner surface of stainless steel tube was the master surface, meanwhile the external surface of core concrete was slave surface. Limited glide was employed in the sliding formulation as well as the discretization method was surface-to-surface. Tangential behavior and normal behavior was defined in contact property to simulate the interfacial bond -glide relationship between stainless steel tube and core concrete. The normal behavior was set to "hard" contact which allows separation after contact. The penalty function was utilized to the friction formula for the tangential behavior. The friction coefficient of 0.5 has been successfully used for simulating low carbon steel CFT columns (Ding *et al*. 2011a, 2014, 2018). According to the reported contents in the reference (Tao *et al*. 2011), although the bond behavior between the stainless steel tube and core concrete are likely to be different compared with that in low carbon steel CFT columns, the bond behavior has very minor influence on the performance of stub columns and the same steel tube-concrete interface model can describe the bond behavior between stainless steel and core concrete. Therefore, the friction coefficient of 0.5 was used to simulate CFSSST stub columns in this study.

A tie constraint may couple two separate surfaces so that no relative motion occurs between them. Therefore, the tie option was chosen for the stainless steel tube, core concrete and loading plate so that the load can be applied to the all specimens in the whole loading process. The loading plate was the master surface as well as the top surface of stainless steel tube and core concrete was the slave surface. Rigid body was used to simulate the loading plate in which the elasticity modulus was taken as 1.0×10^{12} and the Poisson's ratio was set as 1.0×10^{-7}.

A triaxial plastic-damage constitutive model of concrete under axial compression proposed by Ding *et al*. (2011a) was adopted in the model.

$$y=\begin{cases}\dfrac{A_1x+(B_1-1)x^2}{1+(A_1-2)x+B_1x^2} & x\le 1\\[2ex] \dfrac{x}{\alpha_1(x-1)^2+x} & x>1\end{cases} \tag{1}$$

Where A_1 is the ratio of the initial tangent modulus to the secant modulus at peak stress and expresses to $9.1f_{cu}^{-4/9}$; $B_1 = 1.6(A_1 - 1)^2$ is a parameter that controls the decrease in the elastic modulus along the ascending branch of the axial stress-strain relationship. For confined concrete structures, parameter α1 can be taken as 0.15. More parameters of concrete model could be referred to Ding *et al*. (2011a).

The triaxial plastic-damage constitutive model of concrete was based on the stress-strain relation of concrete under uniaxial stress, together with the parameters of concrete strength criterion under multi-axial stresses and other parameters stated while it had no relation to the material and the shape of outer tube (Ding *et al*. 2011a). This concrete model has been validated for circular, square and rectangular low carbon steel CFT stub columns under compression (Ding *et al*. 2011a, 2014, 2018). Since this concrete constitutive model had no relation to the material of tube as well, it was expected that it can be used to simulate the CFSSST stub columns. Therefore, the above

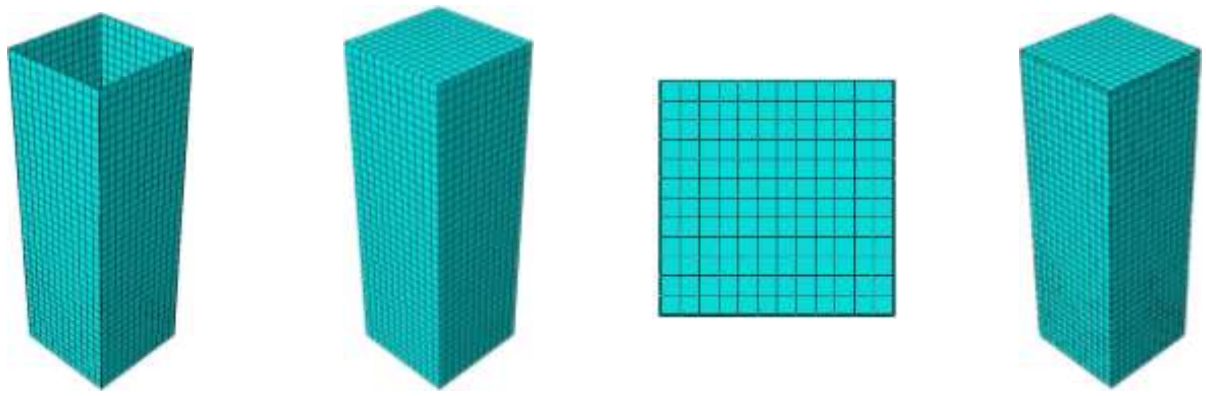

(a) Stainless steel tube (b) Core concrete (c) Loading plate (d)FE model

Fig. 1 Mesh generation of the FE models

stress-strain model of concrete was adopted for simulating CFSSST stub columns. The plastic-damage constitutive model was defined in ABAQUS: the eccentricity is 0.1, the ratio of initial equibiaxial compressive yield stress to initial uniaxial compressive yield stress (f_{b0}/f_{c0}) is 1.225 (Ding *et al*. 2006), the ratio of the second stress invariant on the tensile meridian to that on the compressive meridian is 2/3 (Jankowaik and Lodygowski 2005), the viscosity parameter is 0.0005, the dilation angle is 40° (Ding *et al*. 2006).

The material property of stainless steel is quite different from that of carbon steel due to that stainless steel has no obvious yield stage but has obvious strain-hardening characteristics. Hence a suitable two-stage stainless steel constitutive model proposed by Rasmussen (2003) was adopted in this study.

$$\varepsilon = \begin{cases} \dfrac{\sigma}{E_0} + 0.002\left(\dfrac{\sigma}{\sigma_{0.2}}\right)^n & \sigma \le \sigma_{0.2} \\ \dfrac{\sigma-\sigma_{0.2}}{E_{0.2}} + \varepsilon_u\left(\dfrac{\sigma-\sigma_{0.2}}{\sigma_u-\sigma_{0.2}}\right)^m + \varepsilon_{0.2} & \sigma_{0.2} < \sigma \le \sigma_u \end{cases} \quad (2)$$

Where, in the first stage $\sigma \le \sigma_{0.2}$, the stress-strain relationship of stainless steel is generally represented by the Ramberg-Osgood equation; in the second stage $\sigma_{0.2} < \sigma \le \sigma_u$, the stress-strain relationship of stainless steel is expressed as the equation proposed by Rasmussen (2003). E_0 is the initial elastic modulus of stainless steel; $\sigma_{0.2}$ is the stainless steel yield strength which is defined as the 0.2% proof stress; n is the strain-hardening exponent, which represents the degree of strain hardening of the stainless steel and lower n values indicate the strain hardening behavior becomes more apparent. Various parameters were expressed as follows

$$E_{0.2} = \frac{E_0}{1+0.002n/e}, \qquad e = \frac{\sigma_{0.2}}{E_0},$$

$$\frac{\sigma_{0.2}}{\sigma_u} = \frac{0.2+185e}{1-0.0375(n-5)}, \quad \varepsilon_u = 1-\frac{\sigma_{0.2}}{\sigma_u},$$

$$m = 1+3.5\frac{\sigma_{0.2}}{\sigma_u}, \qquad n = \frac{\ln(20)}{\ln(\sigma_{0.2}/\sigma_{0.01})}$$

Tao *et al*. (2011) reported that the stainless steel model was brief and accurate, which has been successfully adopted to simulate the CFSSST stub columns under axial compression. For simplicity considerations, this model was also used to simulate the CFSSST stub columns under axial compression.

As a contrast, an elasto-plastic model, considering Von Mises yield criteria, Prandtl-Reuss flow rule and isotropic strain hardening, was utilized to describe the constitutive relation of low carbon steel. The expression for the stress-strain relationship of steel was presented by Ding *et al*. (2011a).

$$\sigma_i = \begin{cases} E_s\varepsilon_i & \varepsilon_i \le \varepsilon_y \\ f_s & \varepsilon_y < \varepsilon_i \le \varepsilon_{st} \\ f_s + \zeta E_s(\varepsilon_i - \varepsilon_{st}) & \varepsilon_{st} < \varepsilon_i \le \varepsilon_u \\ f_u & \varepsilon_i > \varepsilon_u \end{cases} \quad (3)$$

Where, σ_i and ε_i are the equivalent stress and strain of low carbon steel respectively. f_s and f_u (= $1.5f_s$) are the yield strength and ultimate strength, respectively. E_s (= 2.06×10^5 MPa) and E_{st} (= ζE_s) are the elastic modulus and strengthening modulus. ε_y, ε_{st} and ε_u are the yield strain, hardening strain and ultimate strain of low carbon steel, which is expressed as $\varepsilon_u = \varepsilon_{st} + 0.5f_s/\zeta E_s$, where $\varepsilon_{st} = 12\varepsilon_y$, $\varepsilon_u = 120\varepsilon_y$ and $\zeta = 1/216$.

Loading was applied in a displacement control mode on the top of a stub column to simulate the axial loading condition. The ends of the stub column were fixed against all degrees of freedom except for the vertical displacement at the top end. In addition, both material and structural nonlinearities were considered in the finite element analysis.

2.2 Model validation

In this paper, the FE models of the CFSSST stub columns under axial compression were verified against the experimental results reported by Uy *et al*. (2011) and Lam and Gardner (2008). The ultimate bearing capacity of FE results were compared with the experimental results in Table 1. It is shown that the average value of the ratios ($N_{u,exp}/N_{u,FE}$) is 0.962 with the corresponding dispersion coefficient of 0.065. The typical load-strain curves of FE results and experimental results were compared as shown in Fig. 2. It can be seen that the ultimate bearing capacity and stiffness obtained from FE results and test results were in good agreement. From the above comparisons, it can be found that generally good agreement is achieved between the FE and test results. Therefore, the FE models can be used to carry out further parametric study of the CFSSST stub columns beyond the range of test specimens.

2.3 Parameter study

Full scale FE models were established to investigate the mechanical behavior of CFSSST stub columns under axial compression. The parameters were described in Table 2, the width of square section B = 600 mm, the columns length L = 1800 mm and the wall-thickness of stainless steel tube t = = 4 mm, 8 mm, 12 mm respectively; austenitic and duplex stainless steel was selected to carried out parameter study, $E_0 = 2.0\times10^5$ MPa, the $\sigma_{0.2}$ of stainless steel is taken as 230 MPa, 350 MPa, 530 MPa respectively, n = 5 to 10 (Eurocode 3 2006); the concrete grades range from 30 MPa to 90 MPa (Eurocode 2 2004). Then, stainless steel and concrete were paired for the square CFSST stub columns: $\sigma_{0.2}$ = 230 MPa was paired with f_c' = 30 MPa, 50 MPa, $\sigma_{0.2}$ = 350 MPa was paired with f_c' = 50 MPa, 70 MPa, $\sigma_{0.2}$ = 530 MPa was paired with f_c' = 70 MPa, 90 MPa. As a contrast, full scale FE models of square low carbon steel CFT stub columns were established and the parameters were the same with CFSSST stub columns except for n. In order to discuss the influence of concrete strength, stainless steel yield strength, steel ratio and strain-hardening exponent, the typical N-ε_L curves were presented in Fig. 3. Figs. 3(a) to (d) illustrate that concrete strength, stainless steel yield strength and steel ratio have significant influence on the

Table 1 Comparison of test results in references and FE results

Specimens	Ref.	$B\times t\times L$ (mm)	E_0 (MPa)	$\sigma_{0.2}$ (MPa)	n	f_{cu} (MPa)	$N_{u,exp}$ (kN)	$N_{u,FE}$ (kN)	$N_{u,exp}/N_{u,FE}$
S20-50×2A	Uy *et al.* (2011)	51×1.81×150	205100	353	10.4	26.9	234	235	0.996
S20-50×2B		51×1.81×150	205100	353	10.4	26.9	243	235	1.034
S30-50×2A		51×1.81×150	205100	353	10.4	43.6	268	251	1.068
S30-50×2B		51×1.81×150	205100	353	10.4	43.6	274	251	1.092
S20-50×3A		51×2.85×150	207900	440	8.2	26.9	358	408	0.877
S20-50×3B		51×2.85×150	207900	440	8.2	26.9	364	408	0.892
S30-50×3A		51×2.85×150	207900	440	8.2	43.6	394	423	0.931
S30-50×3B		51×2.85×150	207900	440	8.2	43.6	393	423	0.929
S20-100×3A		100×2.85×300	195700	358	8.3	26.9	705	761	0.926
S20-100×3B		100×2.85×300	195700	358	8.3	26.9	716	761	0.941
S30-100×3A		100×2.85×300	195700	358	8.3	43.6	765	821	0.931
S30-100×3B		100×2.85×300	195700	358	8.3	43.6	742	821	0.903
S20-100×5A		101×5.05×300	202100	435	7.0	26.9	1352	1454	0.930
S20-100×5B		101×5.05×300	202100	435	7.0	26.9	1348	1454	0.927
S30-100×5A		101×5.05×300	202100	435	7.0	43.6	1434	1511	0.949
S30-100×5B		101×5.05×300	202100	435	7.0	43.6	1461	1511	0.967
S20-150×3A		152×2.85×450	192600	268	6.8	26.9	1035	1079	0.959
S20-150×3B		152×2.85×450	192600	268	6.8	26.9	1062	1079	0.984
S30-150×3A		152×2.85×450	192600	268	6.8	43.6	1074	1305	0.823
S30-150×3B		152×2.85×450	192600	268	6.8	43.6	1209	1305	0.926
S20-150×5A		150×4.80×450	192200	340	5.6	26.9	1804	1815	0.994
S20-150×5B		150×4.80×450	192200	340	5.6	26.9	1798	1815	0.991
S30-150×5A		150×4.80×450	192200	340	5.6	43.6	1947	1814	1.073
S30-150×5B		150×4.80×450	192200	340	5.6	43.6	1976	1814	1.089
SHS-2-C30	Lam *et al.* (2008)	100×2.20×300	202500	385	12.4	37	534	580	0.921
SHS-2-C60		100×2.00×300	202500	385	12.4	66	687	735	0.935
SHS-2-C100		100×2.20×300	202500	385	12.4	92	836	956	0.874
SHS-5-C30		100×5.00×300	180000	458	3.7	37	1410	1348	1.046
SHS-5-C60		100×4.90×300	180000	458	3.7	66	1488	1454	1.023
SHS-5-C100		100×4.90×300	180000	458	3.7	92	1559	1659	0.940
Mean									0.962
Cov									0.065

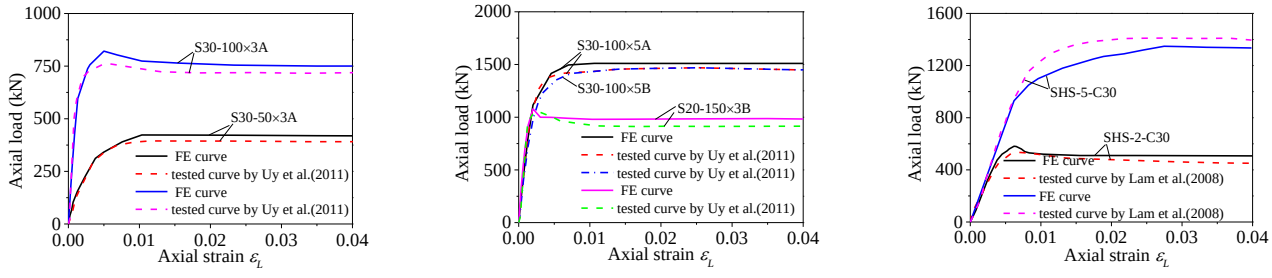

(a) S30-50×3 and S30-100×3 (b) S30-100×5 and S20-150×3 (c) SHS-2-C30 and SHS-5-C30

Fig. 2 Comparison of FE and experimental load-strain curves

ultimate bearing capacity of CFSSST stub columns. In addition, the ultimate bearing capacities of CFSSST stub columns remain almost unchanged when the strain-hardening exponent ranges from 5 to 10, it indicates that mechanical behavior of CFSSST stub columns under axial compression.

Table 2 Varying parameters of specimens for FE parametric study

B (mm)	L (mm)	t (mm)	E_0 (MPa)	n	f_c' (MPa)	$\sigma_{0.2}$ (MPa)
600	1800	4	200000	5,6,7,8,9,10	30, 50	230
		4	200000	5,6,7,8,9,10	50, 70	350
		4	200000	5,6,7,8,9,10	70, 90	530
		8	200000	5,6,7,8,9,10	30, 50	230
		8	200000	5,6,7,8,9,10	50, 70	350
		8	200000	5,6,7,8,9,10	70, 90	530
		12	200000	5,6,7,8,9,10	30, 50	230
		12	200000	5,6,7,8,9,10	50, 70	350
		12	200000	5,6,7,8,9,10	70, 90	530

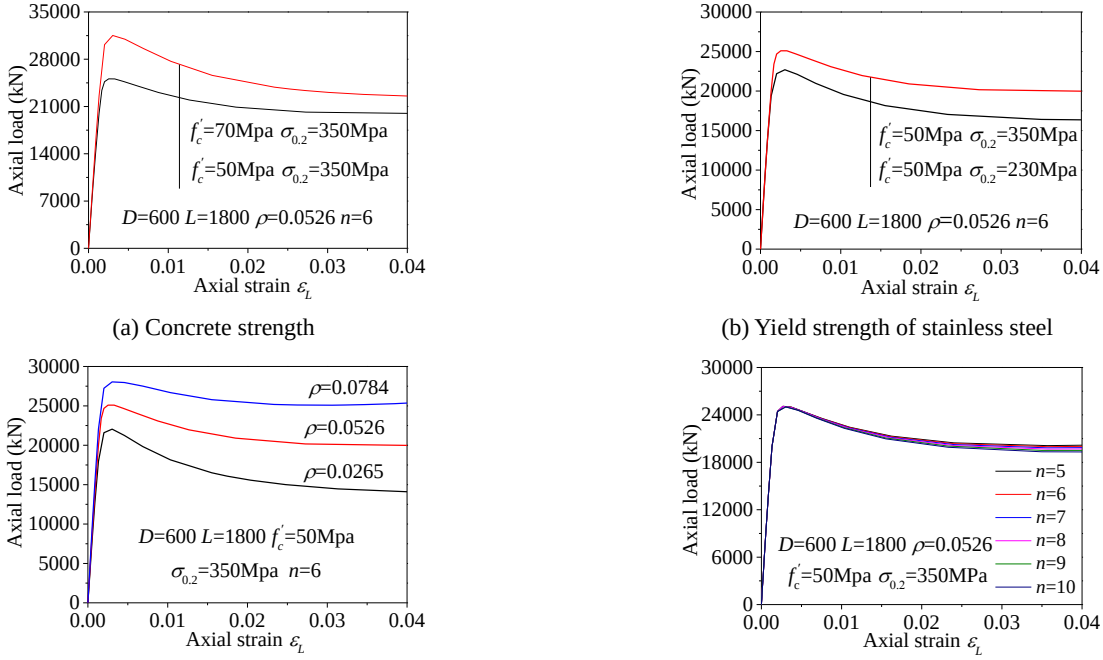

(a) Concrete strength

(b) Yield strength of stainless steel

(c) Steel ratio

(d) Strain-hardening exponent

Fig. 3 Influence of various parameters on the load bearing capacity

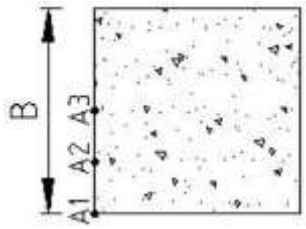

Fig. 4 Cross-sections of FE model

2.4 Composite action analysis

The representative points were selected at end point A1 and middle point A3 on the cross section in the middle height, as presented in Fig. 4, which were aimed to analyze the composite action and its difference for CFSSST stub columns and low carbon steel counterparts. These points were rational for illustrating the composite action as proved in previous studies (Ding *et al*. 2014, 2018).

Fig. 5(a) presents the typical axial stress and transverse stress curves of stainless steel and low carbon steel tube at point A1 and A3. Ding *et al*. (2011b) reported that the axial stress decreases with the increase of transverse stress. If the axial stress curves intersect with the transverse stress, it demonstrates that the degree of composite action is high. Further, the intersection occurs more earlier, the degree of composite action is stronger. The above relationship of axial stress and transverse stress curves has been justified in references (Ding *et al*. 2014, 2018). As shown in Fig. 5(a), the intersection point P1 of stainless steel tube appears earlier than the intersection point P2 of low carbon steel tube at point A1, but there is no intersection of stainless steel tube and low carbon steel tube at the location A3. It is reflected that the composite action at point A1 of stainless steel tube is greater than that of low carbon steel tube while the confinement effect at point A3 for both stainless steel tube and low carbon steel tube is slight. The confinement

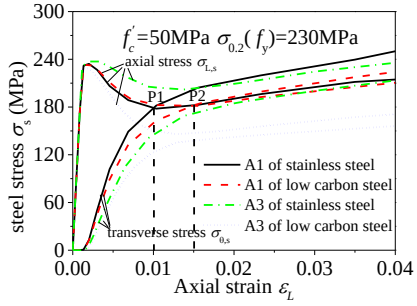

(a) Stress-strain curves of steel tubes

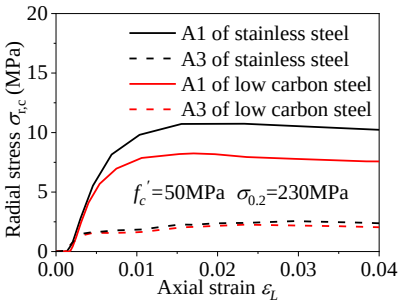

(b) Radial stress-strain curves of core concrete

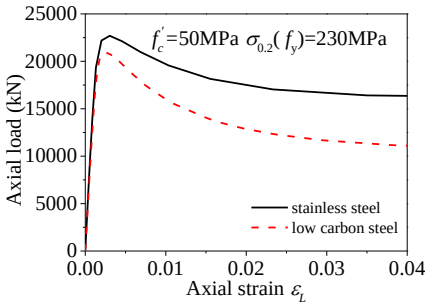

(c) Load-strain (N-ε) curves of steel tubes

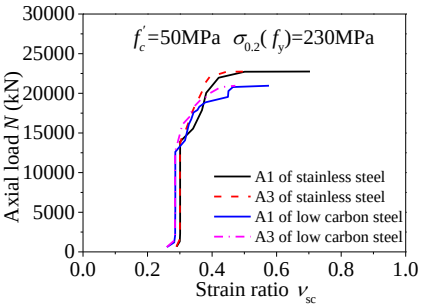

(d) Load-strain ratio (N-ν_{sc}) curves of steel tubes

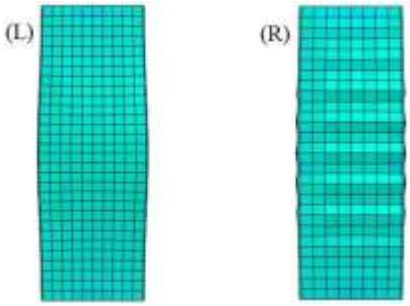

(e) Deformation of CFSSST (L) and low carbon steel CFT (R) columns (ρ = 0.0526)

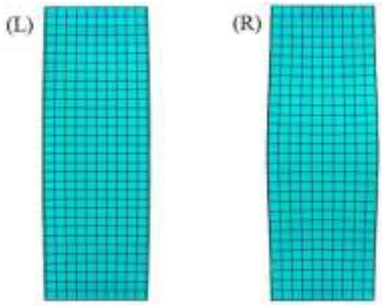

(f) Deformation of CFSSST (L) and low carbon steel CFT (R) columns (ρ = 0.0784)

Fig. 5 Comparison of typical curves for CFSSST and square low carbon steel CFT stub columns

effect for all specimens at the endpoint is greater than that at middle point of the cross-section.

Fig. 5(b) shows the radial stress-strain curves of core concrete in CFSSST stub columns and low carbon steel counterparts. When the CFSSST stub columns and low carbon steel counterparts are axially loaded, both the core concrete and steel tube are subjected to compression until the transverse deformation of concrete exceeds that of steel tube. After that the transverse deformation of core concrete expands increasingly with the continuous loading, which leads to the increase of the radical stress of core concrete and the transverse stress of steel tube duo to confinement effect. The radical stress of core concrete indicates the lateral compressive stress provides by the steel tube on the core concrete. Given by Fig. 5(b), with the same axial strain level, the radical stress of CFSSST stub columns is greater than that of low carbon steel counterparts at point A1 while the radical stress of CFSSST stub columns and low carbon steel counterparts are close and small at point A3. This suggests that the confinement effect of stainless steel tube is greater than that of low carbon steel tube at point A1 and at point A3, the confinement effect is slightly in CFSSST stub columns and low carbon steel counterparts. The composite action for all specimens at endpoint is greater than that at middle point.

As illustrated in Fig. 5(c), it indicates that the load-strain N-ε curves of CFSSST stub columns and low carbon steel counterparts. The confinement effect is better, the bearing capacity is higher and the decreasing degree of bearing capacity is slower. The bearing capacity of CFSSST stub columns is greater than that of low carbon steel counterparts and the decreasing degree of bearing capacity for CFSSST stub columns is slower than that of low carbon steel counterparts. It reflects that the confinement effect of CFSSST stub columns is greater than that of low carbon steel counterparts.

Fig. 5(d) gives the load-strain N-ν_{sc} curves of CFSSST stub columns and low carbon steel counterparts. The ν_{sc} is defined as the absolute value of ratio of transverse strain to axial strain, reflecting the hoop constraint of steel tube exerting on the core concrete. The larger the ν_{sc} is, the stronger the hoop constraint is. It can be seen from Fig. 5(d) that the ν_{sc} of stainless steel tube is larger than that of low carbon steel tube at point A1 and the ν_{sc} of stainless steel

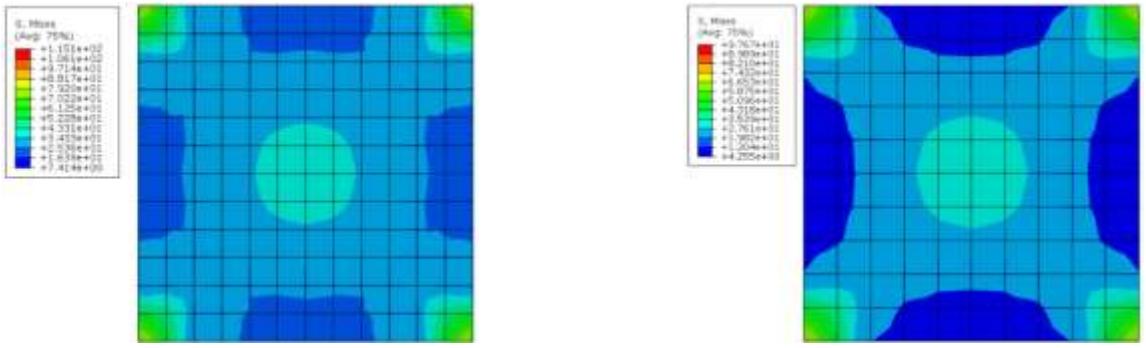

(a) CFSSST stub column (b) Square low carbon steel CFT stub column

Fig. 6 Comparison of stress nephogram at middle section for CFSSST and square carbon steel CFT stub columns

tube and low carbon steel tube are close at point A3 when reaching the ultimate load. The results suggest that CFSSST stub columns have a better confinement effect on the core concrete than low carbon steel counterparts at point A1 and that of CFSSST and low carbon steel CFT stub columns is very weak at point A3.

Figs. 5(e) and (f) present that the failure mode of CFSSST stub columns and low carbon steel counterparts when they reach the ultimate limit state. It can be regarded that the deformation is smaller, the confinement effect is greater. It can be found from Figs. 5(e) and (f) that the deformation of CFSSST stub columns is smaller than that of low carbon steel counterparts when the steel ratio varied. It indicates that the confinement effect of CFSSST columns is greater than that of low carbon steel counterparts.

3. Practical design formula for load bearing capacity

3.1 Model simplification

The FE models were further investigated and the parameters were described as the following: concrete grades ranging from 30 MPa to 90 MPa, yield strength ranging from 230 MPa to 530 Mpa for austenitic and duplex stainless steel and steel ratio ranging from 0.0265 to 0.0784. The stress nephogram at midsection for CFSSST and square low carbon steel CFT stub columns were extracted from the FE modelling as shown in Fig. 6. According to the stress nephogram in Fig. 6, the stress distribution of CFSSST stub columns can be simplified to Fig. 7 for calculation.

The FE modelling results indicates that the confinement effect of CFSSST and square low carbon steel CFT stub columns mainly occurs the corner and middle part of core concrete while it is weaker along with the length of the middle section, as shown in Fig. 6. Due to the composite action of CFSSST stub columns is stronger than that of lower carbon steel counterparts, the constraint area for core concrete of CFSSST stub columns is greater than that of square low carbon steel CFT stub columns, as shown in Table 3.

The model simplification completely keeps to the stress distribution and the superposition theory when the core concrete reaches the ultimate limit state, where assuming

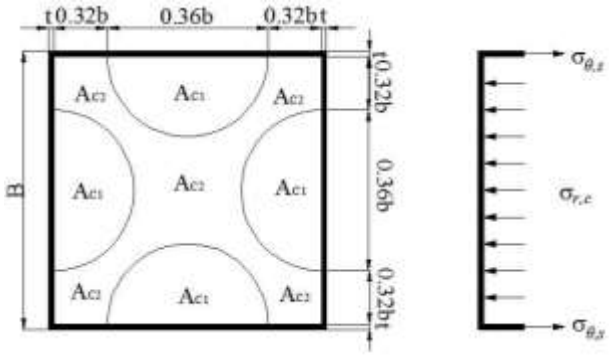

Fig. 7 Simplified stress distribution model at the middle section of CFSSST stub columns

A_{c1} is the unconstrained concrete area, A_{c2} is the constrained concrete area, A_c is the sectional area of the whole core concrete. B is the length of stainless steel tube, b is the width of core concrete and t is the wall-thickness of stainless steel tube, as shown in Fig. 7. The length of unconstrained area A_{c1} is approximately 0.36b according to the stress distribution in Fig. 7. The following relationships can be expressed as

$$\begin{cases} A_{c1} + A_{c2} = A_c \\ A_{c1} = \dfrac{\pi d^2}{2} \end{cases} \tag{4}$$

3.2 Formulation

The axial stress and transverse stress at three points of stainless steel and low carbon steel tube (endpoint A1, 1/4 point A2 and midpoint A3 of middle section as shown in Fig. 4) were obtained from numerical specimens results. The relations between axial stress ($\sigma_{L,s}$)-yield strength ($\sigma_{0.2}$) ratio and the specimen′s ultimate strength ($f_{sc} = N_u/A_{sc}$, $A_{sc} = A_c + A_s$) as well as between transverse stress ($\sigma_{\theta,s}$)-yield strength ($\sigma_{0.2}$) ratio and the specimen′s ultimate strength are shown in Fig. 8.

It can be seen from Figs. 8(a) to (d) that the average ratio of axial stress to yield strength is 1.03 due to the strain-hardening effect of stainless steel tube and the average ratio of transverse stress to yield strength is 0.27 when the CFSSST columns reach the ultimate bearing

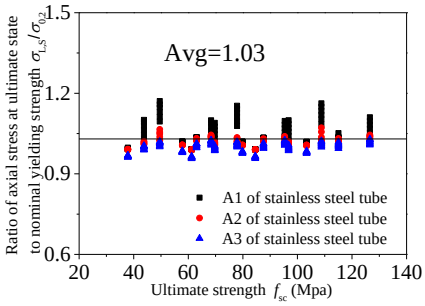

(a) Average ratio of axial compressive stress to yield strength of stainless steel tube

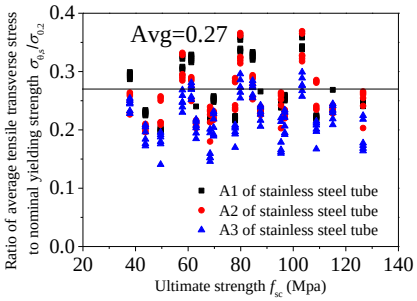

(b) Average ratio of tensile transverse stress to yield strength of stainless steel tube

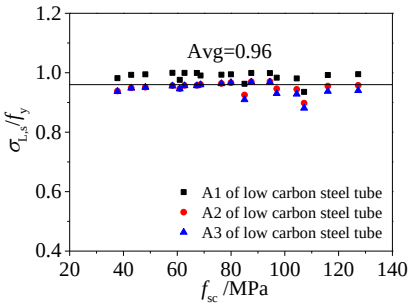

(c) Average ratio of axial compressive stress to yield strength of low carbon steel tube

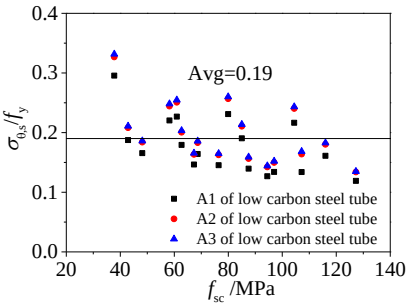

(d) Average ratio of tensile transverse stress to yield strength of low carbon steel tube

Fig. 8 Axial stress and transverse stress of CFSSST and square low carbon steel CFT stub columns

capacity. As a contrast, the average ratio of axial stress to yield strength is 0.96 and the average ratio of transverse stress to yield strength is 0.19 for the square low carbon steel CFT columns. Therefore, it is indicated that the stress contribution of the stainless steel tube is higher that of the corresponding low carbon steel tube.

For CFSSST stub columns, the following expressions are presented, where $\sigma_{0.2}$ is yield strength of stainless steel, A_s is the sectional area of stainless steel tube, $\sigma_{r,c}$ is radial concrete stress of confined area, $\sigma_{L,c}$ is axial compressive stress of core concrete, f_c is uniaxial compressive strength of concrete.

It can be obtained from Fig. 7 and Eq. (4)

$$A_{c1} = 0.20A_c$$
$$A_{c2} = 0.80A_c \tag{5}$$

$$\sigma_{r,c} = \frac{2t\sigma_{\theta,s}}{b} \tag{6}$$

As shown in Figs. 8(a) and (b), when CFSSST stub columns reach the ultimate strength, the average ratio of axial compressive stresss ($\sigma_{L,s}$) to yield strength and tensile transverse stress ($\sigma_{\theta,s}$) to yield strength of stainless steel tube can be obtained as

$$\sigma_{L,s} = 1.03\sigma_{0.2} \tag{7}$$

$$\sigma_{\theta,s} = 0.27\sigma_{0.2} \tag{8}$$

The axial compressive stress ($\sigma_{L,c}$) of constrained core concrete can be given as

$$\sigma_{L,c} = f_c + k\sigma_{r,c} \tag{9}$$

Where k is the coefficient of lateral pressure, k = 3.4 according to Ding *et al*. (2011b).

On the basis of static equilibrium method, the ultimate bearing capacity N_u of axially-loaded CFSSST stub columns can be expressed as

$$N_u = \sigma_{L,c}A_{c2} + f_cA_{c1} + \sigma_{L,s}A_s \tag{10}$$

Substituting Eqs. (5)-(9) into (10), N_u can be obtained as

$$N_u = f_cA_c + K\sigma_{0.2}A_s \tag{11}$$

In Eq. (11), K = 1.4 is the confinement coefficient of CFSSST stub columns, which is greater than K = 1.2 of square low carbon steel CFT stub columns, as shown in Table 3. It reveals that the composite action of CFSSST stub columns is stronger than that of low carbon steel counterparts and the stress contribution of stainless steel is higher than that of low carbon steel.

Table 3 Relationships between the longitudinal stress, transverse stress and yield strength of steel tubes

Type of steel	$\sigma_{L,s}/\sigma_{0.2}(f_y)$	$\sigma_{L,s}/\sigma_{0.2}(f_y)$	A_{c1}/A_c	A_{c2}/A_c	K
Austenitic stainless steel	1.03	0.27	0.2	0.8	1.4
Duplex stainless steel					
Low carbon steel	0.96	0.19	0.25	0.75	1.2

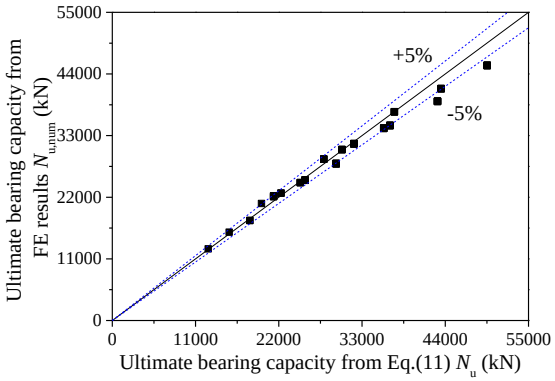

(a) Comparison of the ultimate bearing capacities obtained from FE results and Eq. (11)

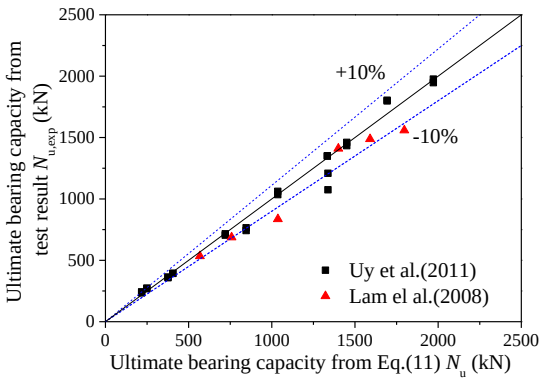

(b) Comparison of the ultimate bearing capacities obtained from test results and Eq. (11)

Fig. 9 Comparisons from FE and test results versus Eq. (11) results

Table 4 Comparison of the numerical results of CFSSST stub columns and Eq. (11)

Specimens	B (mm)	t (mm)	$\sigma_{0.2}$ (MPa)	f_c' (MPa)	n	$N_{u,num}$ (kN)	N_u (kN)	$N_{u,num}/N_u$
C1	600	4	230	30	5	12780	12673	1.008
C2	600	4	230	30	6	12780		1.008
C3	600	4	230	30	7	12780		1.008
C4	600	4	230	30	8	12780		1.008
C5	600	4	230	30	9	12780		1.008
C6	600	4	230	30	10	12780		1.008
C7	600	8	230	30	5	15762	15445	1.021
C8	600	8	230	30	6	15765		1.021
C9	600	8	230	30	7	15767		1.021
C10	600	8	230	30	8	15767		1.021
C11	600	8	230	30	9	15763		1.021
C12	600	8	230	30	10	15757		1.020
C13	600	12	230	30	5	17853	18179	0.982
C14	600	12	230	30	6	17858		0.982
C15	600	12	230	30	7	17860		0.982
C16	600	12	230	30	8	17860		0.982
C17	600	12	230	30	9	17855		0.982
C18	600	12	230	30	10	17845		0.982
C19	600	4	230	50	5	20885	19718	1.059
C20	600	4	230	50	6	20887		1.059
C21	600	4	230	50	7	20888		1.059
C22	600	4	230	50	8	20888		1.059
C23	600	4	230	50	9	20886		1.059
C24	600	4	230	50	10	20882		1.059
C25	600	8	230	50	5	22748	22300	1.020
C26	600	8	230	50	6	22751		1.020
C27	600	8	230	50	7	22753		1.020
C28	600	8	230	50	8	22753		1.020
C29	600	8	230	50	9	22748		1.020
C30	600	8	230	50	10	22726		1.019

Table 4 Continued

Specimens	B (mm)	t (mm)	$\sigma_{0.2}$ (MPa)	f_c' (MPa)	n	$N_{u,num}$ (kN)	N_u (kN)	$N_{u,num}/N_u$
C31	600	12	230	50	5	24604	24847	0.990
C32	600	12	230	50	6	24609		0.990
C33	600	12	230	50	7	24611		0.991
C34	600	12	230	50	8	24611		0.991
C35	600	12	230	50	9	24606		0.990
C36	600	12	230	50	10	24596		0.990
C37	600	4	350	50	5	22139	21320	1.038
C38	600	4	350	50	6	22133		1.038
C39	600	4	350	50	7	22125		1.038
C40	600	4	350	50	8	22265		1.044
C41	600	4	350	50	9	22256		1.044
C42	600	4	350	50	10	22093		1.036
C43	600	8	350	50	5	25090	25483	0.985
C44	600	8	350	50	6	25082		0.984
C45	600	8	350	50	7	25073		0.984
C46	600	8	350	50	8	25060		0.983
C47	600	8	350	50	9	25029		0.982
C48	600	8	350	50	10	25006		0.981
C49	600	12	350	50	5	28053	29589	0.948
C50	600	12	350	50	6	28038		0.948
C51	600	12	350	50	7	28019		0.947
C52	600	12	350	50	8	27994		0.946
C53	600	12	350	50	9	27965		0.945
C54	600	12	350	50	10	27930		0.944
C55	600	4	350	70	5	28817	27943	1.031
C56	600	4	350	70	6	28812		1.031
C57	600	4	350	70	7	28805		1.031
C58	600	4	350	70	8	28796		1.031
C59	600	4	350	70	9	28785		1.030
C60	600	4	350	70	10	28773		1.030
C61	600	8	350	70	5	31582	31929	0.989
C62	600	8	350	70	6	31570		0.989
C63	600	8	350	70	7	31557		0.988
C64	600	8	350	70	8	31539		0.988
C65	600	8	350	70	9	31518		0.987
C66	600	8	350	70	10	31496		0.986
C67	600	12	350	70	5	34344	35860	0.958
C68	600	12	350	70	6	34329		0.957
C69	600	12	350	70	7	34309		0.957
C70	600	12	350	70	8	34293		0.956
C71	600	12	350	70	9	34281		0.956
C72	600	12	350	70	10	34262		0.955
C73	600	4	530	70	5	30524	30347	1.006
C74	600	4	530	70	6	30516		1.006
C75	600	4	530	70	7	30508		1.005
C76	600	4	530	70	8	30499		1.005
C77	600	4	530	70	9	30491		1.005

Table 4 Continued

Specimens	B (mm)	t (mm)	$\sigma_{0.2}$ (MPa)	f_c' (MPa)	n	$N_{u,num}$ (kN)	N_u (kN)	$N_{u,num}/N_u$
C78	600	4	530	70	10	30480	30347	1.004
C79	600	8	530	70	5	34842	36703	0.949
C80	600	8	530	70	6	34829		0.949
C81	600	8	530	70	7	34816		0.949
C82	600	8	530	70	8	34801		0.948
C83	600	8	530	70	9	34785		0.948
C84	600	8	530	70	10	34767		0.947
C85	600	12	530	70	5	39164	42972	0.911
C86	600	12	530	70	6	39147		0.911
C87	600	12	530	70	7	39128		0.911
C88	600	12	530	70	8	39108		0.910
C89	600	12	530	70	9	39087		0.910
C90	600	12	530	70	10	39064		0.909
C91	600	4	530	90	5	37271	37286	1.000
C92	600	4	530	90	6	37264		0.999
C93	600	4	530	90	7	37256		0.999
C94	600	4	530	90	8	37248		0.999
C95	600	4	530	90	9	37239		0.999
C96	600	4	530	90	10	37230		0.998
C97	600	8	530	90	5	41416	43455	0.953
C98	600	8	530	90	6	41404		0.953
C99	600	8	530	90	7	41391		0.953
C100	600	8	530	90	8	41376		0.952
C101	600	8	530	90	9	41360		0.952
C102	600	8	530	90	10	41344		0.951
C103	600	12	530	90	5	45559	49541	0.920
C104	600	12	530	90	6	45543		0.919
C105	600	12	530	90	7	45525		0.919
C106	600	12	530	90	8	45505		0.919
C107	600	12	530	90	9	45485		0.918
C108	600	12	530	90	10	45463		0.918
		Mean						0.987
		COV						0.041

3.3 Formula validation

The FE modelling results ($N_{u,num}$) for all CFSSST stub columns were compared with the predicted results (N_u) by Eq. (11), as shown in Table 4 and Fig. 9(a). The average ratio of $N_{u,num}$ to N_u is 0.987 with the corresponding dispersion coefficient of 0.041. It can be found from Table 5 that the predicted the bearing capacities were also calculated by EC4, ACI-318 and CECS-159, where f_c' is the compressive concrete cylinder strength, A_c is the cross-sectional area of the concrete, A_s is the cross-sectional area the steel tube, f_c is the uniaxial compressive concrete strength and f_y has been taken equal to the 0.2% proof strength $\sigma_{0.2}$ of stainless steel. In addition, $f_c = 0.4f_{cu}^{7/6}$ (Ding *et al*. 2011a) and the conversion between f_{cu} and f_c' presented by Chen *et al*. (1992)

Table 5 Summary of available formulas in well-known national codes

References	formulas	Remarks
EC4(2004)	$N_{EC4} = f_yA_s + f_c'A_c$	
ACI-318 (2011)	$N_{ACI} = f_yA_s + 0.85f_c'A_c$	Square
CECS-159 (2004)	$N_{CECS} = f_yA_s + f_cA_c$	

$$f_c' = \begin{cases} 0.8f_{cu} & f_{cu} \le 50MPa \\ f_{cu} - 10 & f_{cu} > 50MPa \end{cases}$$

As shown in Fig. 9(b) and Table 6, the experimental results were compared with those predicted by Eq. (11) and other design methods. The average ratio of $N_{u,exp}$ to N_u is

Table 6 Comparison between experimental and predicted results using different design methods

Specimens	Ref.	$N_{u,exp}$ (kN)	N_u (kN)	N_{EC4} (kN)	N_{ACI} (kN)	N_{CECS} (kN)	$N_{u,exp}$ /N_u	$N_{u,exp}$ /N_{EC4}	$N_{u,exp}$ /N_{ACI}	$N_{u,exp}$ /N_{CECS}
S20-50×2A	Uy *et al.* (2011)	234	218	174	167	167	1.075	1.345	1.401	1.401
S20-50×2B		243	218	174	167	167	1.116	1.397	1.455	1.455
S30-50×2A		268	249	204	192	199	1.075	1.314	1.396	1.347
S30-50×2B		274	249	204	192	199	1.099	1.343	1.427	1.377
S20-50×3A		358	376	286	279	280	0.951	1.252	1.283	1.279
S20-50×3B		364	376	286	279	280	0.967	1.273	1.305	1.300
S30-50×3A		394	405	313	302	309	0.972	1.259	1.305	1.275
S30-50×3B		393	405	313	302	309	0.97	1.256	1.301	1.272
S20-100×3A		705	720	588	559	562	0.979	1.199	1.261	1.254
S20-100×3B		716	720	588	559	562	0.994	1.218	1.281	1.274
S30-100×3A		765	846	707	660	687	0.904	1.082	1.159	1.114
S30-100×3B		742	846	707	660	687	0.877	1.050	1.124	1.080
S20-100×5A		1352	1334	1021	994	997	1.013	1.324	1.360	1.356
S20-100×5B		1348	1334	1021	994	997	1.01	1.320	1.356	1.352
S30-100×5A		1434	1451	1131	1088	1113	0.989	1.268	1.318	1.288
S30-100×5B		1461	1451	1131	1088	1113	1.007	1.292	1.343	1.313
S20-150×3A		1035	1036	916	847	854	0.999	1.130	1.222	1.212
S20-150×3B		1062	1036	916	847	854	1.025	1.159	1.254	1.244
S30-150×3A		1074	1338	1203	1091	1156	0.803	0.893	0.984	0.929
S30-150×3B		1209	1338	1203	1091	1156	0.904	1.005	1.108	1.046
S20-150×5A		1804	1694	1372	1308	1315	1.065	1.315	1.379	1.372
S20-150×5B		1798	1694	1372	1308	1315	1.062	1.310	1.375	1.367
S30-150×5A		1947	1972	1636	1533	1592	0.988	1.190	1.270	1.223
S30-150×5B		1976	1972	1636	1533	1592	1.002	1.208	1.289	1.241
SHS-2-C30	Lam *et al.* (2008)	534	568	505	463	481	0.940	1.057	1.153	1.110
SHS-2-C60		687	758	654	584	630	0.906	1.051	1.176	1.090
SHS-2-C100		836	1037	908	805	874	0.806	0.921	1.039	0.957
SHS-5-C30		1410	1400	1087	1050	1066	1.007	1.297	1.343	1.323
SHS-5-C60		1488	1591	1235	1174	1214	0.936	1.205	1.267	1.226
SHS-5-C100		1559	1797	1431	1341	1401	0.868	1.089	1.163	1.113
Mean							0.977	1.201	1.270	1.240
COV							0.079	0.107	0.088	0.104

0.977 with the corresponding dispersion coefficient of 0.079. The average ratio of $N_{u,exp}$ to N_{EC4}, N_{ACI} and N_{CECS} is 1.201, 1.270 and 1.240 with the corresponding dispersion coefficient is 0.107; 0.088 and 0.104 respectively. Therefore, the proposed formula (Eq. (11)) has higher accuracy compared with other design methods and it is therefore adopted for predicting the ultimate bearing capacity of CFSSST stub columns.

4. Conclusions

This paper investigates the confinement coefficient for concrete-filled square stainless steel tubular (CFSSST) stub columns under axial loading. Parameter study on the composite action between the stainless steel tube and core concrete was conducted using the FE models that were validated by existing experimental results. Furthermore, the composite action of CFSSST stub columns were compared with that of carbon steel counterparts. A practical calculation formula was proposed to predict the ultimate

bearing capacity of CFSSST stub columns and verified against the test results. Base on the above work of this study, the following conclusions can be drawn:

- Based on a triaxial plastic-damage concrete constitutive relations with features of the parameter certainty and a rational stainless steel constitutive model, a fine finite 3D solid element model of CFSSST stub columns was established. The FE results are good agreement with the test results and it indicates the FE modelling is valid and feasible.
- A parametric study focusing on the full scale CFSSST stub columns were performed based on the validated FE modelling technique. The FE results reveal that the composite action of CFSSST stub columns is stronger than that of their carbon steel counterparts.
- The FE analysis results indicate that the average ratio of axial stress to yield strength is 1.03 due to the strain-hardening effect of stainless steel tube and the average ratio of transverse stress to yield strength is 0.27 when the CFSSST columns reach the ultimate bearing capacity. As a contrast, the average ratio of axial stress to yield strength is 0.96 and the average ratio of transverse stress to yield strength is 0.19 in the low carbon steel square CFT columns. Therefore, it is indicated that the stress contribution of stainless steel in CFSSST stub columns is higher than that of the low carbon steel counterparts.
- The stress nephogram of core concrete was simplified properly and a calculation formula to predict the ultimate bearing capacity of CFSSST stub columns was proposed based on superposition method. In the proposed formula, the confinement coefficient of CFSSST stub columns is 1.4, which is greater than the confinement coefficient of 1.2 for the low square carbon steel CFT stub columns. The proposed formula has higher accuracy compared with other design methods. Therefore, it is suggested to be used for predicting the bearing capacity of CFSSST stub columns in engineering practice.

Acknowledgments

This research is supported by the National Key Research Program of China, Grant No. 2017YFC0703404, and the National Natural Science Foundation of China, Grant No. 51608538.

References

ACI 318-11 (2011), Building Code Requirements for Structural Concrete and Commentary ACI Committee 318; American Concrete Institute, Detroit, MI, USA.

CECS 159 (2004), Technical Specification for Structures with Concrete-Filled Rectangular Steel Tube Members; China Association for Engineering Construction Standardization, Beijing, China.

Chen, Z.Y., Zhu, J.Q. and Wu, P.G. (1992), *High-strength Concrete and Its Applications*, Tsinghua University Press, Beijing, China. [In Chinese]

Ding, F.X. and Yu, Z.W. (2006), "Strength criterion for plain concrete under multiaxial stress based on damage Poisson's ratio", *Acta Mech. Solid. Sin.*, **19**(4), 307-316.

Ding, F.X., Ying, X.Y., Zhou, L.C. and Yu, Z.W. (2011a), "Unified calculation method and its application in determining the uniaxial mechanical properties of concrete", *Front. Archit. Civil Eng. China*, **5**(3), 381.

Ding, F.X., Yu, Z.W., Bai, Y. and Gong, Y.Z. (2011b), "Elasto-plastic analysis of circular concrete-filled steel tube stub columns", *J. Constr. Steel Res.*, **67**(10), 1567-1577.

Ding, F.X., Fang, C.J., Bai, Y. and Gong, Y.Z. (2014), "Mechanical performance of stirrup-confined concrete-filled steel tubular stub columns under axial loading", *J. Constr. Steel Res.*, **98**, 146-157.

Ding, F.X., Luo, L., Zhu, J., Wang, L.P. and Yu, Z.W. (2018), "Mechanical behavior of stirrup-confined rectangular CFT stub columns under axial compression", *Thin-Wall. Struct.*, **124**, 136-150.

Ellobody, E. and Ghazy, M.F. (2013), "Polypropylene fibre reinforced concrete-stainles steel composite columns: design and behavior", *Adv. Struct. Eng.*, **16**(3), 427-440.

Eurocode 2 (2004), Design of Concrete Structures, part 1-1: General Rules and Rules for Buildings; British Standards Institution, London, UK.

Eurocode 3 (2006), Design of Steel Structure, part 1-4: General Rules—Supplementary Rules for Stainless Steel; BS EN 1993-1-4, British Standards Institution, London, UK.

Eurocode 4 (2004), Design of Steel Composite Steel and Concrete Structures, part 1-1: General Rules and Rules for Building; BS EN 1994-1-1, British Standards Institution, London, UK.

Evirgen, B., Tuncan, A. and Taskin, K. (2014), "Structural behavior of concrete filled steel tubular sections (CFT/CFST) under axial compression", *Thin-Wall. Struct.*, **80**(9), 46-56.

Gedge, G. (2008), "Structural uses of stainless steel — buildings and civil engineering", *J. Constr. Steel Res.*, **64**(11), 1194-1198.

Han, L.H., Chen, F., Liao, F.Y., Tao, Z. and Uy, B, (2013), "Fire performance of concrete filled stainless steel tubular columns", *Eng. Struct.*, **56**(6), 165-181.

Jankowaik, T. and Lodygowski, T. (2005), "Identification of parameters of concrete damage plasticity constitutive model", *Found. Civ. Environ. Eng.*, **6**, 53-69.

Lam, D. and Gardner, L. (2008), "Structural design of stainless steel concrete filled columns", *J. Constr. Steel Res.*, **64**(11), 1275-1282.

Li, N., Lu, Y.Y., Li, S. and Liang, H.J. (2015), "Statistical-based evaluation of design codes for circular concrete-filled steel tube columns", *Steel Compos. Struct., Int. J.*, **18**(2), 519-546.

Liao, F.Y., Han, L.H., Tao, Z. and Rasmussen, K.J.R. (2016), "Experimental behavior of concrete-filled stainless steel tubular columns under cyclic lateral loading", *J. Struct. Eng.*, **143**(4), 04016219.

Lume, G., Rasmussen, K.J.R., Tao, Z. and Han, L.H. (2017), "Experimental behaviour of high-strength thin-walled concrete filled steel tubular stub columns", *Ce/papers*, **1**(2-3), 1976-1985.

Patel, V.I., Liang, Q.Q. and Hadi, M.N.S. (2014), "Nonlinear analysis of axially loaded circular concrete-filled stainless steel tubular short columns", *J. Constr. Steel Res.*, **101**(101), 9-18.

Patton, M.L. and Singh, K.D. (2014), "Finite element modelling of concrete-filled lean duplex stainless steel tubular stub columns", *Int. J. Steel Struct.*, **14**(3), 619-632.

Pons, D., Espinós, A., Albero, V. and Romero, M.L. (2018), "Numerical study on axially loaded ultra-high strength concrete-filled dual steel columns", *Steel Compos. Struct., Int. J.*, **26**(6).

Rasmussen, K.J.R. (2003), "Full-range stress–strain curves for stainless steel alloys", *J. Constr. Steel Res.*, **59**(1), 47-61.

Tam, V.W.Y., Wang, Z.B. and Tao, Z. (2014), "Behaviour of

recycled aggregate concrete filled stainless steel stub columns", *Mater*. *Struct*., **47**(1-2), 293-310.
Tao, Z., Uy, B., Liao, F.Y. and Han, L.H. (2011), "Nonlinear analysis of concrete-filled square stainless steel stub columns under axial compression", *J*. *Constr*. *Steel Res*., **67**(11), 1719-1732.
Uy, B., Tao, Z. and Han, L.H. (2011), "Behaviour of short and slender concrete-filled stainless steel tubular columns", *J*. *Constr*. *Steel Res*., **67**(3), 360-378.
Wan, C.Y. and Zha, X.X. (2016), "Nonlinear analysis and design of concrete-filled dual steel tubular columns under axial loading", *Steel Compos*. *Struct*., *Int*. *J*., **20**(3), 571-597.
Yang, Y., Zhou, J., Wei, J., Huang, L., Wu, Q. and Chen, B. (2016), "Experimental study on the compression of concrete filled steel tubular latticed columns with variable cross section", *Steel Compos*. *Struct*., *Int*. *J*., **22**(3), 663-675.

DL